Marine Safe Propulsion Simulation: Can loop-shaped propellers reduce marine animal laceration injuries?

Computational Research Prototype
Tom Teasdale
EcoVision Analytics

Research Question

Do loop-shaped propellers plausibly reduce laceration-risk proxies relative to conventional propellers under matched wildlife-encounter simulations? The short answer is yes, with important limits. Strongest support comes from the laceration/contact submodel, where loop-shaped propellers reduce exposed-edge and edge-severity terms under matched encounter draws. The rotating-sweep tissue-surrogate runs agree: after merging RPM levels, loop-shaped contact yields lower peak strain, stress, strain-energy density, and high-strain tissue volume at both tested contact depths. CFD is secondary—the sliding-mesh matrix shows lower mean absolute pressure, turbulent kinetic energy, dissipation, and eddy viscosity for loop-shaped geometry, but modestly higher mean velocity. Loop-shaped propellers may therefore reduce modeled laceration risk primarily through geometry and edge-contact mechanisms; they do not yet prove a universal reduction in all hydrodynamic risk mechanisms or a validated biological injury reduction.

Scope and Interpretation

Manatee and giant manta ray surrogate scenarios are compared in one laceration-focused framework using imported conventional and loop-shaped CAD propeller geometries. The aggregate score excludes blunt-force injury because the motivating question is propeller-cut/laceration risk rather than blunt trauma. All numerical outputs are comparative simulation proxies, not validated injury probabilities or mortality predictions—best read as hypothesis-generating guidance for CFD, contact experiments, and expert review.

1 Shared Model Architecture

Five mechanisms are treated separately: encounter/contact probability, laceration potential, hydrodynamic exposure, animal behavior state, and aggregation. A loop-shaped propeller should not be assumed to reduce every mechanism uniformly; it can soften exposed cutting-edge severity while leaving local velocity unchanged or even higher.

1.1 Encounter Sampling

For each Monte Carlo draw i, the framework samples boat speed V_b, propeller speed N in revolutions per minute, animal swimming speed V_a, approach angle θ, longitudinal offset x, lateral offset y, and vertical offset z. Behavior state s_i is sampled from a categorical distribution:

$$P(s_i = s) = \frac{w_s}{\sum_j w_j},$$

where w_s is the literature-informed prior weight for behavior state s. Behavior states modify orientation, avoidance, and local offset distributions.

1.2 Contact Model

Radial offset from the propeller axis is

$$r = \sqrt{y^2 + z^2}.$$

The animal is considered geometrically exposed to the disk when r lies within the propeller radius plus an animal-clearance term. The number of rotations during the encounter is approximated as

$$R_e = \frac{N}{60}\, t_d,$$

where t_d is the time in the propeller disk. The phase/contact term is

$$P_\phi = 1 - \exp(-c_\phi\, B\, R_e\, E_t),$$

where c_ϕ is the phase-contact coefficient, B is blade or loop count, and E_t is the exposed-tip/contact factor. The continuous contact likelihood is then

$$L_c = \mathrm{clamp}(P_\phi\, D_c\, M_b),$$

where D_c is the normalized contact-depth proxy and M_b is the behavior/avoidance modifier. A contact event is registered when the disk-overlap condition is true and L_c exceeds the configured contact threshold.

1.3 Laceration Model

The laceration model is active only when contact occurs. Relative speed combines axial encounter speed and tangential blade/loop speed at the modeled propeller contact radius:

$$r_c = \min(\max(r, r_h), R_p),$$

where R_p is propeller radius. The relative speed proxy is

$$V_{\mathrm{rel}} = \sqrt{V_{\mathrm{axial}}^2 + \left(2\pi r_c \frac{N}{60}\right)^2},$$

where r_h is hub radius. Edge severity combines a dimensionless sharpness term S_e and a bluntness term derived from leading-edge radius R_e^{edge}:

$$E_c = \text{clamp}\left(0.65S_e + 0.35\,\text{clamp}\left(\frac{1}{R_e^{edge}}\right)\right).$$

The laceration energy proxy is

$$E_l = \text{clamp}\left(0.55\frac{V_{\text{rel}}}{12} + 0.45D_c\right),$$

and the laceration score is

$$L = \text{clamp}(E_l\, E_c\, M_m\, M_r),$$

where M_m is a mass-scaling factor and M_r is a contact-region tissue modifier. The explicit test is whether a loop-shaped design that lowers E_t, lowers S_e, and increases effective leading-edge radius also lowers L under matched encounter draws.

1.4 Heuristic Weighting Coefficients

Several contact and laceration coefficients are engineering assumptions, not experimentally calibrated tissue or propeller parameters. They keep each submodel bounded and laceration-focused and should not be read as fitted biological constants.

Edge-contact severity uses a 0.65/0.35 sharpness-to-bluntness split; laceration-energy uses 0.55/0.45 velocity-to-depth weighting (velocity normalized by $12\,\text{m}\,\text{s}^{-1}$ as a reference scale, not a tissue-failure threshold). Post hoc sweeps over 50/50–90/10 splits moved laceration-proxy reduction by less than 1 percentage point because the CAD-derived sharpness gap between geometries dominates the comparison. Matched encounters share the same velocity and depth realizations, so energy weights barely affect percent reduction. The aggregate score $0.80L + 0.20H$ is intentionally laceration-focused; varying that split to 50/50–90/10 shifts combined-score reduction by roughly 7 percentage points without changing the laceration-proxy reduction.

1.5 Hydrodynamic Proxy and Aggregation

Hydrodynamic exposure is retained as secondary context, not as a direct laceration measure. It combines pressure, wake, and shear proxies:

$$H = \text{clamp}(0.42P_h + 0.33W_h + 0.25S_h).$$

The active aggregate score is laceration-focused:

$$A = \text{clamp}(0.80L + 0.20H).$$

Because L receives 80% of the aggregate weight, the main scientific question remains laceration/contact mechanics; CFD checks for contradictory flow signals rather than replacing the laceration submodel.

1.6 Matched-Encounter Design

Conventional and loop-shaped propellers are evaluated on the same sampled encounters. For a metric X, the reported percent reduction is

$$\Delta_X = 100\frac{X_{\text{conv}} - X_{\text{loop}}}{X_{\text{conv}}}.$$

Matching encounters reduces sampling noise and isolates geometry and mechanism-specific terms.

2 Computational Tools and Reproducibility

The simulation and postprocessing workflow was implemented in Python, OpenFOAM, and FEBio. Python was used for encounter sampling, laceration/contact proxy evaluation, geometry normalization, finite-element case generation, CSV/JSON outputs, and scientific plotting. OpenFOAM was used for first-pass finite-volume CFD scaffolds and transient incompressible sliding-mesh flow solves. FEBio was used for finite-element tissue-surrogate contact calculations. The computational environment used for this report included NumPy 2.5.1, SciPy 1.18.0, pandas 3.0.3, Matplotlib 3.11.0, trimesh 4.12.2, Pydantic 2.13.4, PyYAML 6.0.3, Typer 0.26.8, pytest 9.1.1, OpenFOAM 13, and FEBio 4.12.0.

Tool	Role in this study
NumPy/SciPy	Numerical arrays, random sampling, vectorized metric calculations, and scientific-computing primitives.
pandas	Tabular Monte Carlo results, behavior-state summaries, CFD field summaries, and report-ready CSV outputs.
Matplotlib	Static scientific figures for laceration proxies, behavior weighting, CFD distributions, and CFD metric ratios.
trimesh	STL import/export, mesh normalization, propeller scaling, animal surrogate geometry, and surface diagnostics.
Pydantic/PyYAML	Configuration validation and structured model inputs from YAML files.
OpenFOAM	Finite-volume CFD mesh generation and transient incompressible sliding-mesh flow solution around paired propeller/animal geometries.
FEBio	Finite-element tissue-surrogate contact simulations for paired conventional and loop-shaped rotating-sweep contact.
pytest	Regression tests for configuration loading, geometry generation, model outputs, report generation, and CFD scaffolds.

Table 1: Computational tools used in the reproducible prototype workflow.

Package references are included because the claim depends on a reproducible workflow, not only on biological and fluid-dynamics assumptions.

3 CAD-Derived Geometry Measurements

The laceration model uses CAD-measured proxy profiles generated from the imported STL meshes. These measured profiles are the geometry inputs reported here. They are not a substitute for manufacturer drawings or physical edge-radius measurements, but they provide a reproducible, geometry-resolved basis for the paired comparison.

3.1 Measurement Procedure

All geometry metrics were extracted in Python with `trimesh` from normalized STL meshes using the script `scripts/measure_cad_profiles.py`. The workflow was:

1. Load the STL mesh and, if needed, concatenate scene geometry into a single watertight surface.

2. Translate the mesh centroid to the origin and rotate the shortest bounding-box axis onto the propeller shaft ($+z$).
3. Scale the mesh so that the maximum planar extent matches the study radius $R_p = 0.28\,\mathrm{m}$.
4. Compute projected planform area as $\sum_i |n_{z,i}| A_i/2$, where n_z is the face normal and A_i is face area; divide by πR_p^2 to obtain a projected-area ratio. The factor of 1/2 reduces double counting from opposing faces in thin closed meshes.
5. Estimate hub radius as the 15th percentile of vertex radial distance in the propeller plane.
6. Estimate leading-edge radius from localized circle fits on outer mesh sections: at several axial levels, identify leading-edge candidate vertices in radial wedges and fit a circle to each local neighborhood. If section fitting fails, fall back to an axial-thickness proxy.
7. Map edge-radius estimate to a bounded sharpness score with a monotone decreasing function; larger inferred radius yields lower sharpness.
8. For loop-shaped geometry, estimate aperture ratio as 1− projected-area ratio, clipped to a plausible open-loop range.

Section-based circle fitting uses the imported STL mesh geometry directly and is stronger than the earlier thickness-only proxy, but it is still mesh-derived rather than physical metrology. Physical propeller scans, manufacturer CAD sections, or coordinate-measuring-machine measurements remain the preferred validation source.

Measured proxy	Conventional CAD propeller	Loop-shaped
Mesh vertices	742	235313
Mesh faces	1492	470137
Projected area ratio proxy	0.840	0.357
Hub radius proxy (m)	0.054	0.078
Edge radius (mm)	5.40	7.37
Edge radius method	section_circle_fit	section_circle_fit
Thickness fallback (mm)	1.50	7.23
Loop aperture proxy	–	0.643

Table 2: CAD-measured proxy geometry inputs used for the measured-profile laceration rerun.

The conventional propeller shows a higher projected-area proxy and sharper exposed-edge proxy; the loop-shaped propeller shows a lower projected-area proxy, a larger section-fitted leading-edge radius, and an open-aperture geometry that lowers modeled exposed cutting-edge contact. Those differences drive the lower laceration proxy in the matched simulations, though section-fitted mesh radii still require validation against manufacturer CAD sections or physical edge metrology.

4 Laceration Model Audit

The large laceration-proxy reduction was audited with matched-encounter Monte Carlo diagnostics rather than unpaired summary means alone. Within each draw, conventional and loop-shaped propellers share boat speed, RPM, animal position, orientation, and behavior state. The per-draw difference is

$$d_i = L_{i,\mathrm{conv}} - L_{i,\mathrm{loop}},$$

with nonparametric bootstrap intervals over d_i—a numerical uncertainty check on the estimator, not validation against field injury data.

Scenario	Conv. L	Loop L	Reduction	95% CI	Loop lower	Contact Δ	Edge Δ	Energy Δ
Manatee	0.282	0.107	61.8%	61.0–62.7%	0.953	0.053	0.444	0.038
Giant Manta Ray	0.234	0.087	63.0%	61.8–64.4%	0.757	0.060	0.447	0.045

Table 3: Paired laceration-model audit. Contact, edge, and energy deltas are conventional minus loop-shaped means.

Interestingly, contact-rate differences are small while the edge-contact-factor gap is large. The CAD-measured loop-shaped propeller therefore reduces the laceration proxy through lower edge-severity/contact geometry, not through substantially fewer predicted encounters.

Scenario	Propeller	Contact rate	Rel. speed	Edge factor	Edge-contact	Energy	L
Manatee	Conventional	0.953	46.3	0.780	0.742	0.852	0.282
Manatee	Loop-shaped	0.900	46.5	0.320	0.298	0.813	0.107
Giant Manta Ray	Conventional	0.757	51.1	0.780	0.750	0.657	0.234
Giant Manta Ray	Loop-shaped	0.697	51.8	0.320	0.303	0.612	0.087

Table 4: Mechanism-term summary used to diagnose the source of the laceration-proxy reduction. Relative speed is averaged over contact events.

Strict predictive accuracy cannot yet be estimated without labeled ground-truth outcomes. For now, the relevant checks are estimator precision, matched-design consistency, sensitivity to edge-radius and sharpness assumptions, threshold robustness, geometry-measurement repeatability, and comparison against future tank-test or field data.

5 Sensitivity to Weighting and Geometry Assumptions

Many reported reductions cluster near 60–70%. That pattern is real, but it is not primarily caused by fixed weighting coefficients.

A post hoc weighting sweep varied the edge-contact split (50/50 to 90/10), the velocity/depth energy split (50/50 to 90/10), and the aggregate laceration/hydrodynamic split (50/50 to 90/10). Laceration-proxy reduction remained 61.1–62.3% for manatees and 62.3–63.5% for giant manta rays across all edge-weight and energy-weight combinations tested. Combined-score reduction varied more (34–56%) when the aggregate split changed, because hydrodynamic terms receive larger relative weight. One surprising result came from geometry measurement rather than weight tuning: upgrading edge-radius estimation from thickness-only proxies to section-based circle fits dropped the laceration reduction from about 78% to about 62% as the conventional propeller's inferred leading-edge radius rose from 1.5 mm to 5.4 mm.

One-factor-at-a-time sensitivity over uncertain geometry and encounter assumptions shows where the result is fragile. For manatees, loop-shaped edge sharpness and conventional leading-edge sharpness produced the widest combined-proxy ranges (about 0.11 each). The weakest loop-shaped advantage occurred when loop sharpness was stressed to 0.7, yielding a 46% combined-proxy reduction rather than the 72% baseline; loop-shaped still scored lower than conventional in every scenario tested.

The report therefore stands or falls mainly on edge-geometry realism, not on whether default coefficients were exactly 0.65/0.35 or 0.80/0.20. Future work should prioritize physical edge-radius measurement, tissue-surrogate calibration, and conservative geometry stress tests rather than fine-tuning heuristic weights alone.

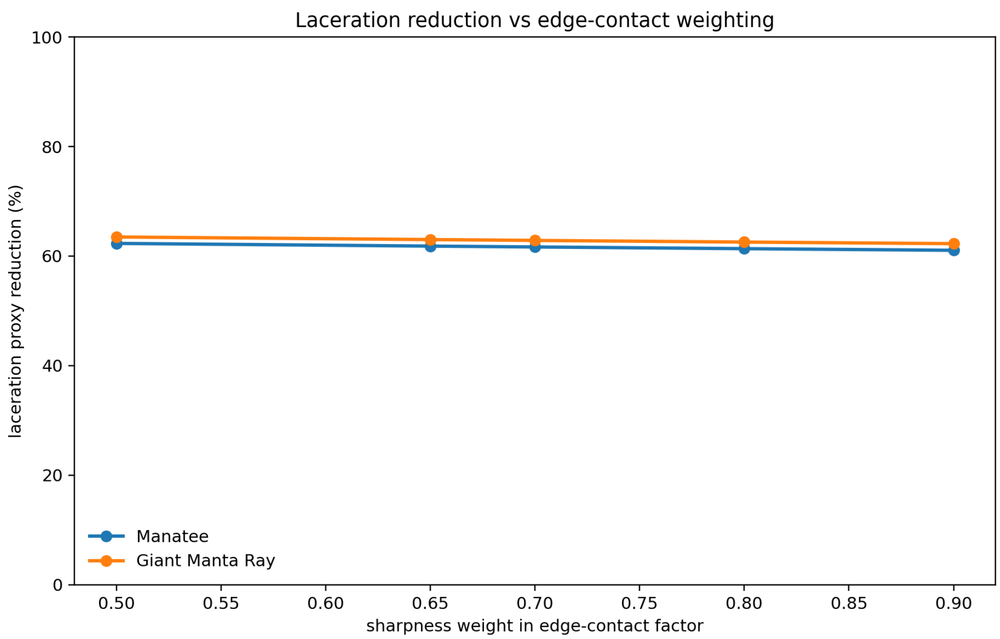

Figure 1: Post hoc sensitivity of laceration-proxy reduction to the sharpness/bluntness split in the edge-contact factor. The result is stable because geometry-derived sharpness differs much more between propellers than the weighting split does.

6 Manatee

6.1 Baseline Laceration-Focused Comparison

Under matched Monte Carlo draws, the laceration proxy falls from 0.282 to 0.107 (61.8% reduction); combined score reduction is 50.4%. Contact probability is 5.3 percentage points lower for the loop-shaped propeller.

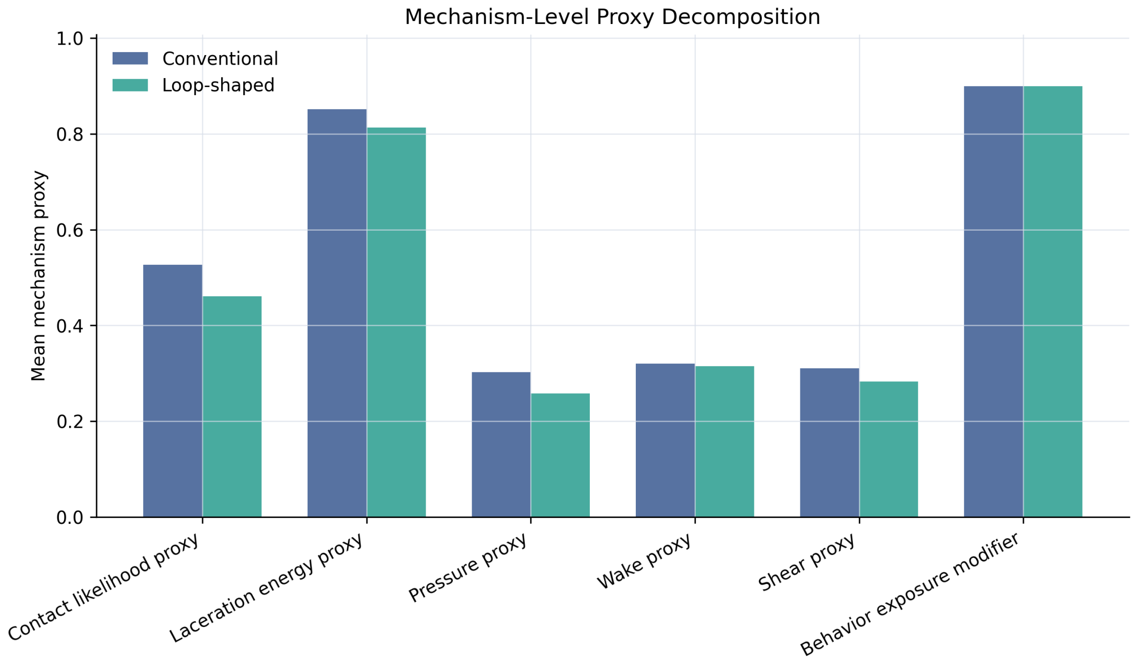

Figure 2: Mechanism decomposition for Manatee.

6.2 Behavior-Weighted Exposure

Behavior state	Sample fraction	Laceration proxy	Weighted laceration contribution
resting_near_surface	0.365	0.320	0.117
grazing_transit	0.286	0.290	0.083
surfacing_to_breathe	0.162	0.321	0.052

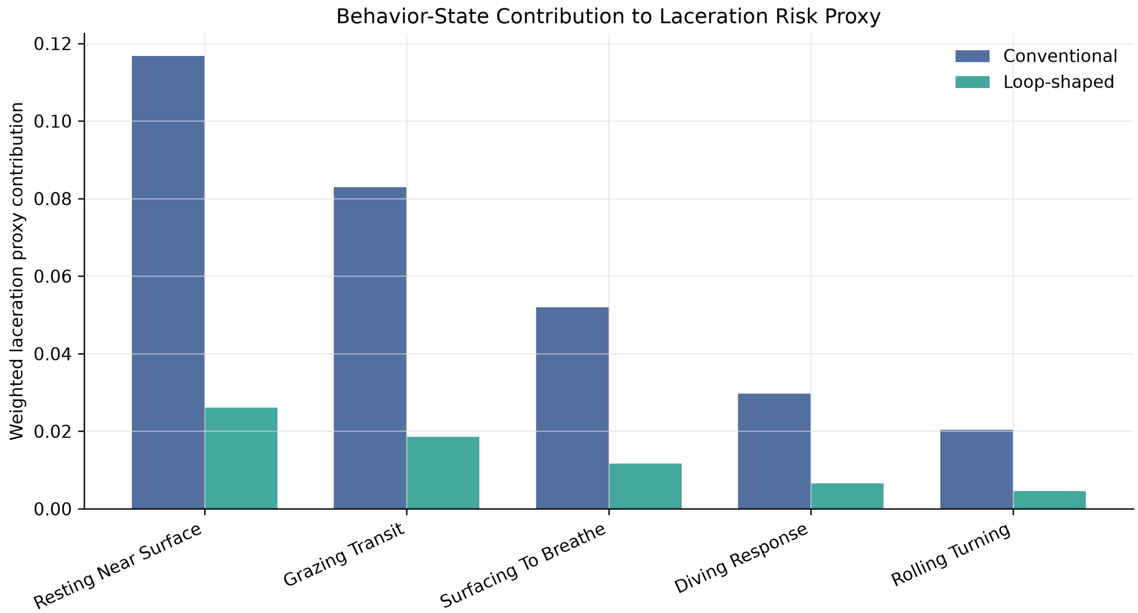

Figure 3: Behavior-state contribution to the laceration proxy for Manatee.

6.3 Orientation Sensitivity

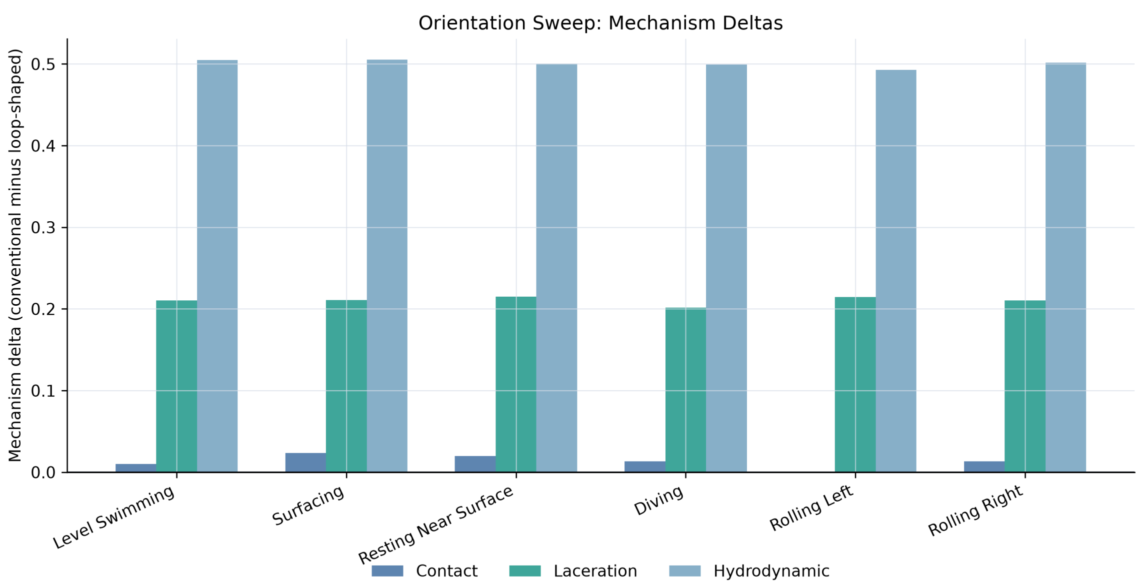

Figure 4: Orientation mechanism deltas for Manatee.

7 Giant Manta Ray

7.1 Baseline Laceration-Focused Comparison

Under matched Monte Carlo draws, the laceration proxy falls from 0.234 to 0.087 (63.0% reduction); combined score reduction is 52.6%. Contact probability is 6.0 percentage points lower for the loop-shaped propeller.

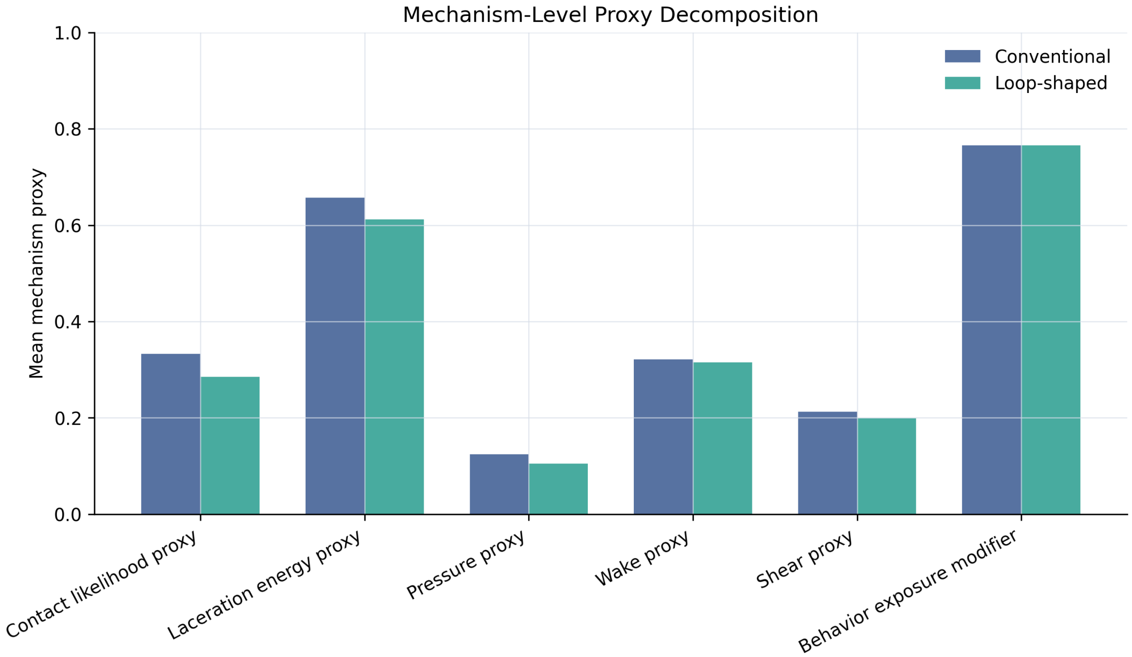

Figure 5: Mechanism decomposition for Giant Manta Ray.

7.2 Behavior-Weighted Exposure

Behavior state	Sample fraction	Laceration proxy	Weighted laceration contribution
cruising	0.337	0.252	0.085
surface_feeding	0.249	0.254	0.063
banked_turning	0.177	0.272	0.048

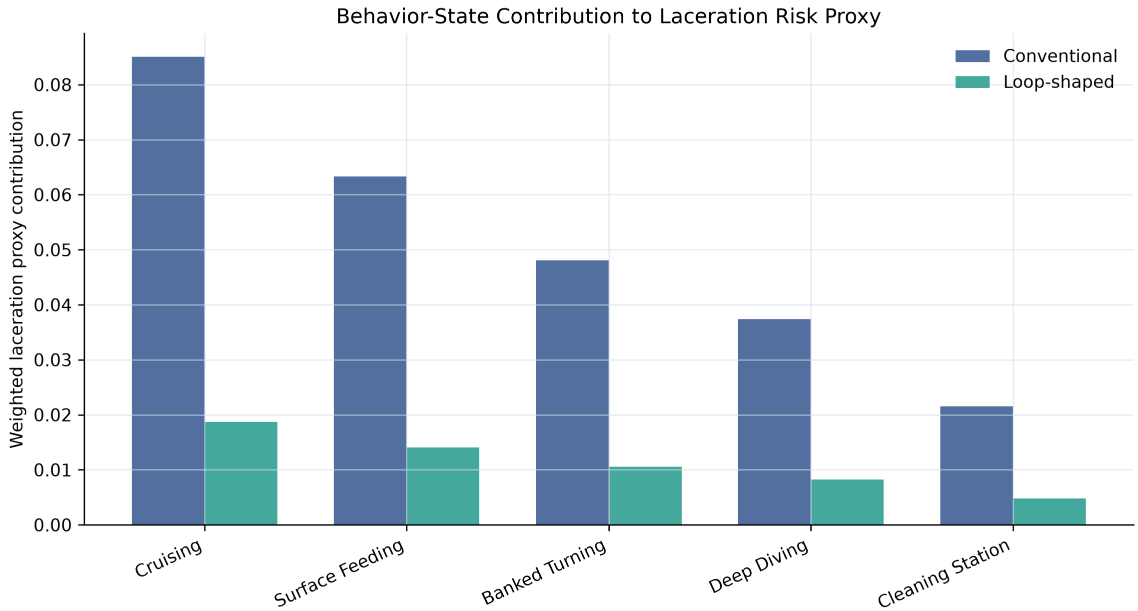

Figure 6: Behavior-state contribution to the laceration proxy for Giant Manta Ray.

7.3 Orientation Sensitivity

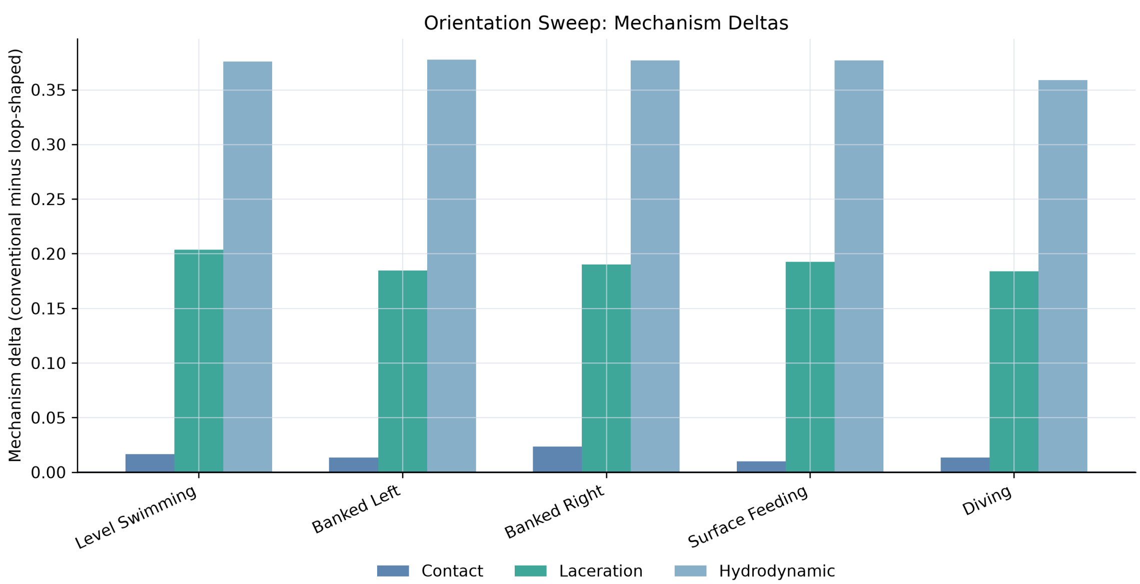

Figure 7: Orientation mechanism deltas for Giant Manta Ray.

8 Interpretation of Laceration Risk

In both species scenarios, loop-shaped propellers score lower on the laceration proxy under matched draws, driven mainly by edge-contact severity rather than large contact-rate differences. CFD contributes only a secondary hydrodynamic check: cutting requires contact with a loaded edge, and flow-field averages alone cannot establish whether tissue is cut.

The defensible chain is

loop-shaped geometry → lower modeled edge-contact severity → lower laceration proxy,

with finite-element tissue loading and future contact experiments needed before stronger biological claims are warranted.

9 Selected CFD Encounter Cases

Cases are selected from the highest behavior-weighted laceration contributors for each species and organized as matched conventional/loop-shaped comparisons in the CFD matrix.

Species	Behavior	Propeller	Lac. score	Pair Lac. Δ
manatee	resting_near_surface	Conventional	0.320	0.248
manatee	resting_near_surface	Loop-shaped	0.072	–
manatee	grazing_transit	Conventional	0.290	0.225
manatee	grazing_transit	Loop-shaped	0.065	–
giant_manta_ray	cruising	Conventional	0.252	0.197
giant_manta_ray	cruising	Loop-shaped	0.056	–
giant_manta_ray	surface_feeding	Conventional	0.254	0.198
giant_manta_ray	surface_feeding	Loop-shaped	0.056	–

The pair laceration delta is the conventional score minus the loop-shaped score for the same behavior state, shown once per pair.

10 Sliding-Mesh CFD Matrix

The transient sliding-mesh matrix includes 12 matched CFD comparisons: two species, two behavior states per species, and three RPM levels at 1750, 3500, and 6000 RPM. Each comparison evaluates both propellers over one modeled revolution and summarizes 18 nonzero written time frames. Older static and MRF runs are retained only as development history and are not interpreted as report results.

Metric	Time-mean	Case range	Final-frame mean	Conv. mean	Loop mean
Mean $\|p\|$	-36.9%	-45.3% to -27.8%	-37.1%	3.88	2.41
Mean k	-32.2%	-41.9% to -23.1%	-27.4%	0.18	0.119
Mean $\|U\|$	+2.5%	+1.6% to +4.4%	+2.7%	4.27	4.38
Mean ϵ	-48.2%	-61.2% to -36.0%	-33.9%	9.21	4.75
Mean ν_t	-2.9%	-8.7% to -1.1%	-2.7%	0.00232	0.00225

Table 8: Loop-shaped percent difference relative to conventional sliding-mesh field means across all 12 paired comparisons. Negative values indicate lower loop-shaped field values.

Across the full sliding-mesh matrix, loop-shaped geometry shows lower mean absolute kinematic pressure, turbulent kinetic energy, dissipation, and slightly lower eddy viscosity. Unexpectedly, mean velocity magnitude is modestly higher—so the hydrodynamic picture is mechanism-specific rather than uniformly favorable. Several turbulence- and pressure-related exposure proxies fall while local speed through the sampled domain rises slightly, which is broadly compatible with a laceration story driven by edge geometry rather than bulk flow reduction.

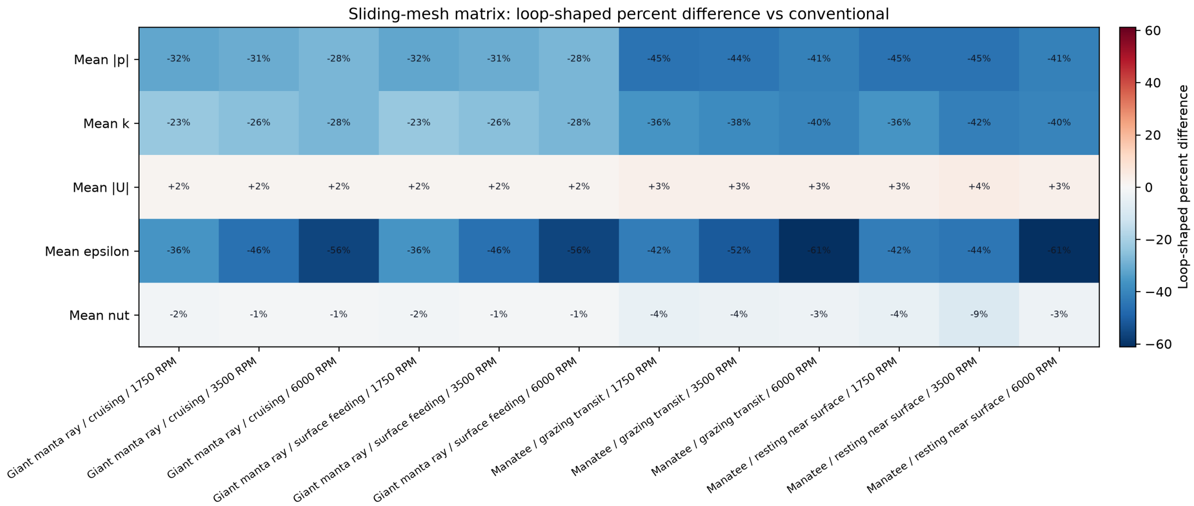

Figure 8: Sliding-mesh CFD matrix heatmap. Values are loop-shaped percent differences relative to conventional time-mean field values; negative values indicate lower loop-shaped values.

11 Rotating-Sweep Tissue-Surrogate Contact Model

FEBio compares conventional and loop-shaped contact under matched rotating-sweep conditions rather than treating laceration as a purely abstract edge score. Each condition used the same imposed contact depth and rotational speed for both geometries; postprocessing extracted maximum-over-time tissue loading rather than only the final frame.

11.1 Rationale for Tissue-Loading Proxies

Four quantities were extracted: p95 absolute principal strain, p95 absolute principal stress, p95 strain-energy density, and tissue volume above principal-strain thresholds. Laceration is a localized material-failure process, so principal strain captures the strongest local tensile deformation, principal stress gives a complementary severity indicator, strain-energy density integrates local deformation intensity, and high-strain volume thresholds summarize affected area (with greater threshold sensitivity than the continuous p95 metrics). These are comparative loading indicators for later mapping to cut/no-cut or cut-depth outcomes in tissue-surrogate experiments, not calibrated injury laws.

Rotational speed was evaluated at 1750, 3500, and 6000 RPM. Interestingly, after merging across RPM, geometry and contact depth dominated the pattern rather than rotational speed. At 4 mm imposed contact, loop-shaped geometry reduced p95 strain by 43.5%, p95 stress by 54.7%, p95 strain-energy density by 70.5%, and tissue volume above strain 0.10 by 78.6%. At 8 mm, the corresponding reductions were 33.6%, 49.6%, 70.8%, and 46.3%; tissue volume above strain 0.25 was reduced by 100% in the merged summary.

$$\Delta_X(D) = 100\frac{\overline{X}_{\mathrm{conv}}(D) - \overline{X}_{\mathrm{loop}}(D)}{\overline{X}_{\mathrm{conv}}(D)},$$

where D is imposed contact depth and $\overline{X}$ is the value of proxy X after merging across the tested RPM levels.

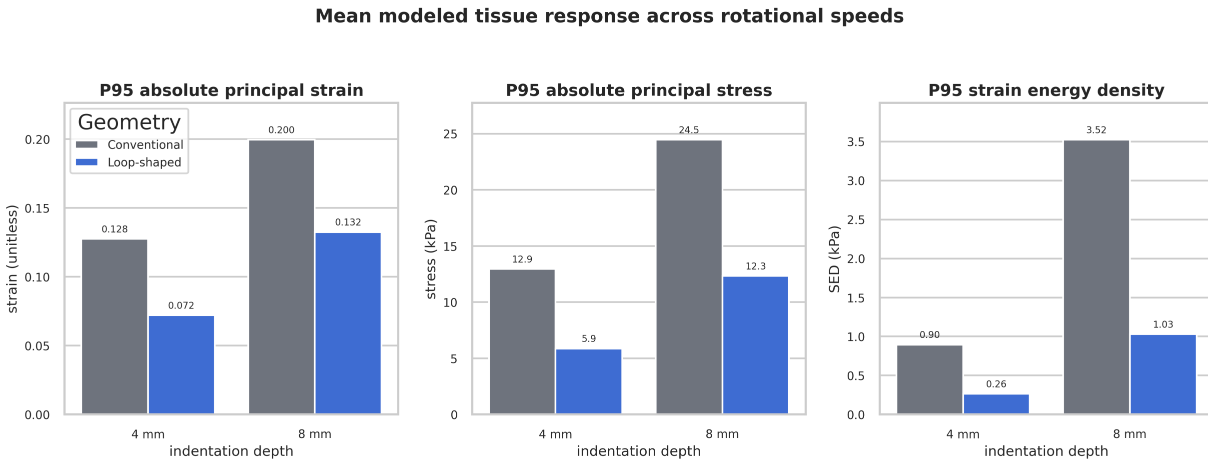

Figure 9: Merged rotating-sweep tissue-surrogate laceration-severity proxies by contact depth. Values are summarized across the tested RPM levels, emphasizing the geometry and depth effects rather than RPM-specific traces.

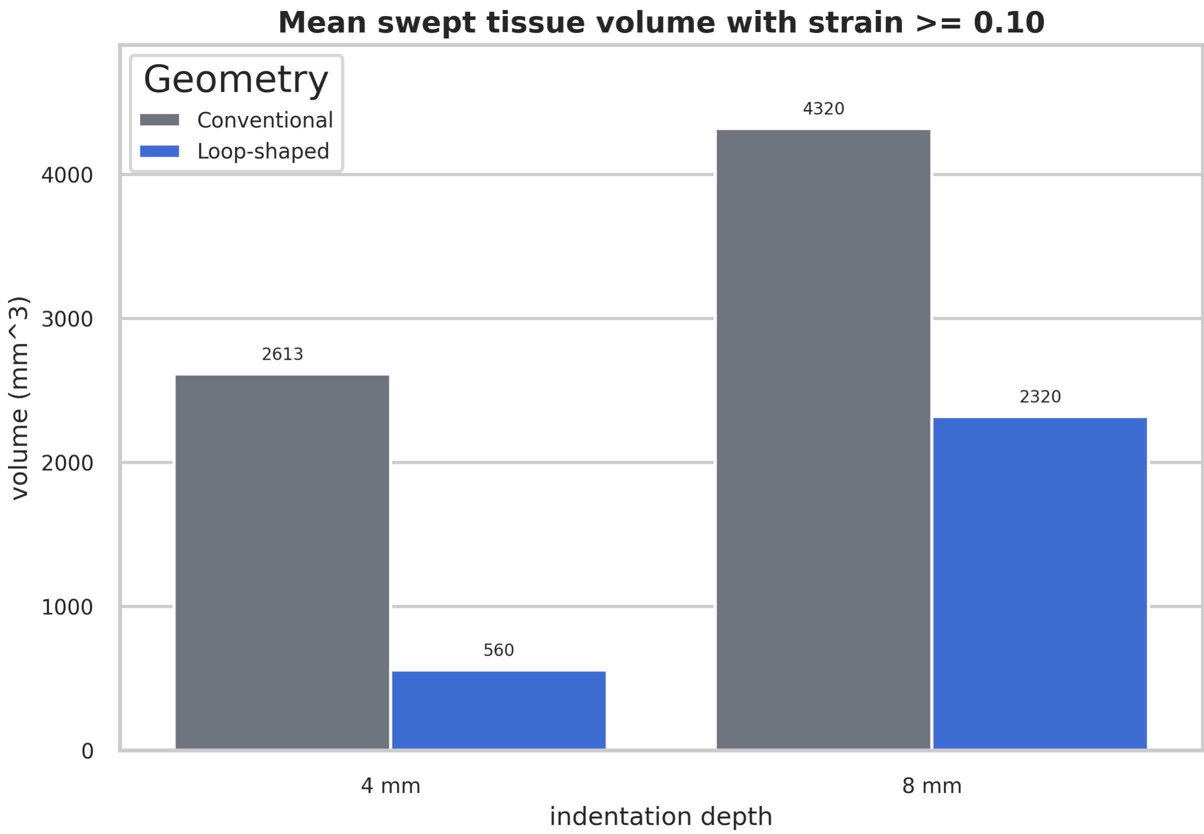

Figure 10: Merged high-strain tissue-volume proxies by contact depth. The loop-shaped geometry produces a smaller volume of tissue above the selected strain thresholds in the paired tissue-surrogate model.

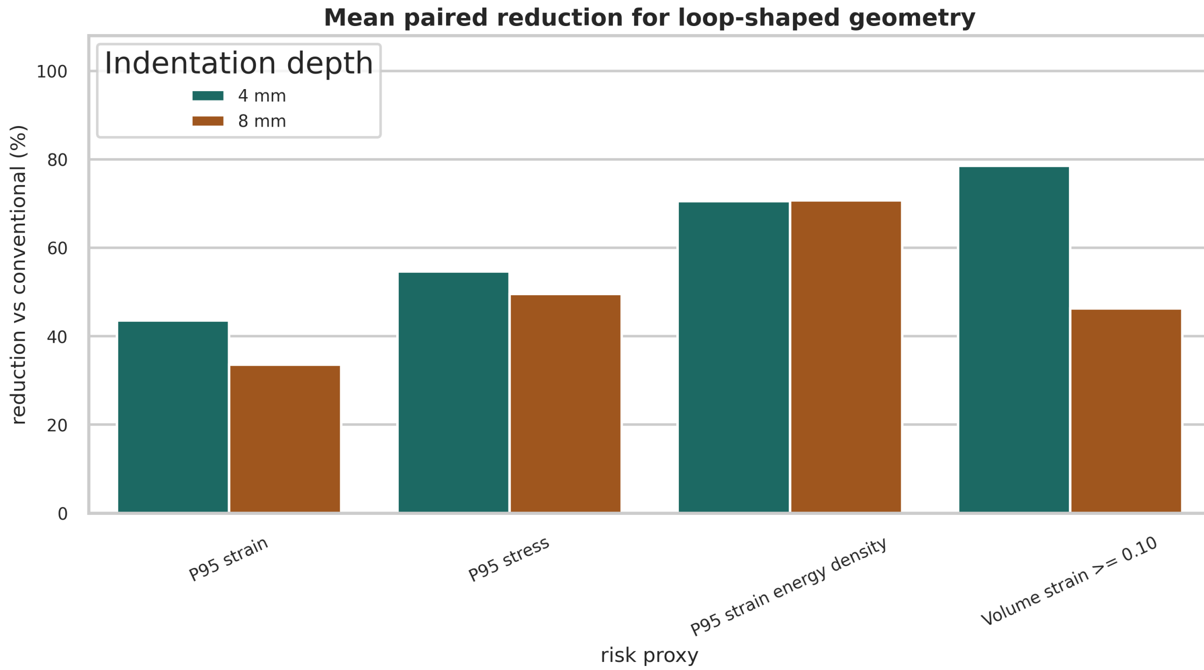

Figure 11: Merged paired percent reductions for loop-shaped contact relative to conventional contact. Positive values indicate lower loop-shaped tissue-loading proxies after RPM levels are combined.

Finite-element contact aligns with the earlier laceration proxy: loop-shaped geometry yields lower concentrated tissue-loading proxies under matched conditions. Strain-energy density remains the most stable reduction (approximately 70–71% at both depths); high-strain tissue volume is more depth-sensitive. Loop-shaped contact appears to distribute or soften loading in the surrogate, reducing the concentration of deformation associated with laceration severity.

11.2 Tissue-Surrogate Material Sensitivity

With species-specific tissue failure properties unavailable, the FEBio contact runs were bracketed across surrogate-material assumptions while holding geometry, contact depth, contact time, and representative rotational speed constant. Loop-shaped contact remained lower for the main tissue-loading proxies across the matrix. Median reductions were 36.1% for p95 principal strain, 68.9% for p95 strain-energy density, and 54.6% for tissue volume above principal strain 0.10. Volume above strain 0.25 had a median reduction of 78.9% but was less stable because many simulations produced little tissue above that higher threshold. Continuous loading proxies look robust; threshold-volume summaries depend more on the chosen damage threshold and contact depth.

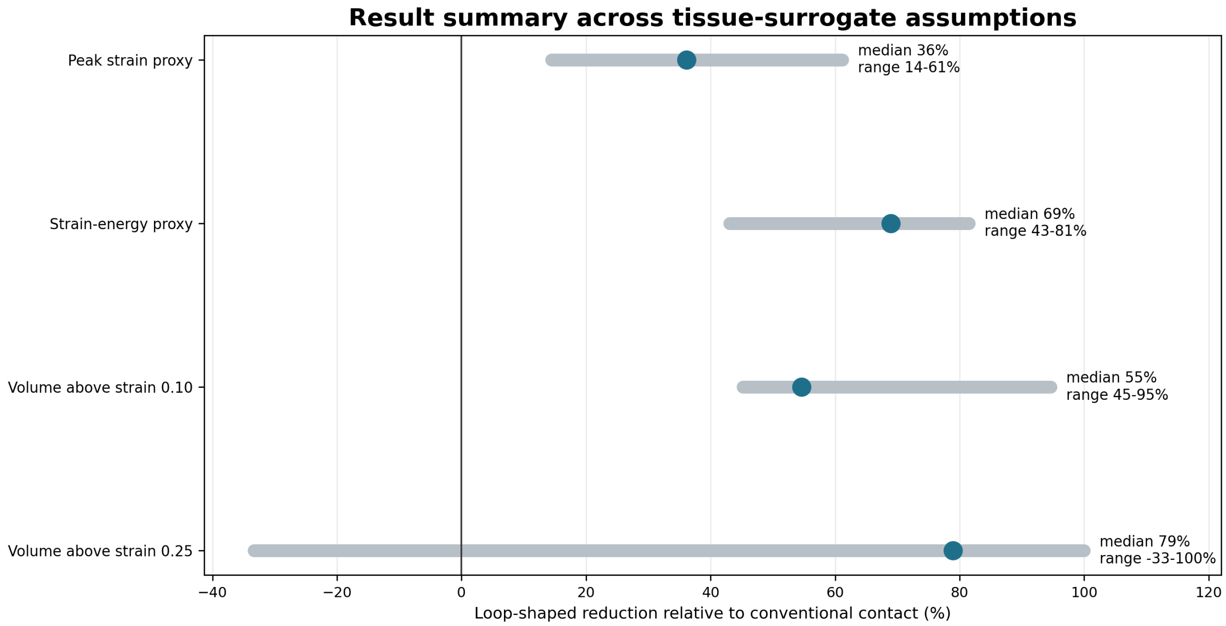

Figure 12: Material-sensitivity ranges for paired loop-shaped reductions relative to conventional contact. Lines show min-to-max ranges across tissue-surrogate assumptions; diamonds mark medians.

11.3 Severe-Depth Contact Sweep

Imposed contact depths of 4, 8, 12, and 16 mm were tested at 3500 RPM to probe the boundary of the laceration-reduction claim, not to imply that real wounds are limited to these depths. Two surrogate-material settings were retained: nominal soft tissue and a stiffer superficial layer.

Loop-shaped contact remained lower for the main continuous proxies, but the effect weakened and became less smooth at the most severe depths. Across eight depth/material cases, p95 strain was 4–44% lower and p95 strain-energy density was 6–71% lower; volume above strain 0.10 was generally lower but threshold-sensitive in the deepest stiff-layer case. A compact mesh-refinement diagnostic at 12 and 16 mm showed that loop-shaped reductions in p95 strain and strain-energy density persisted under refinement.

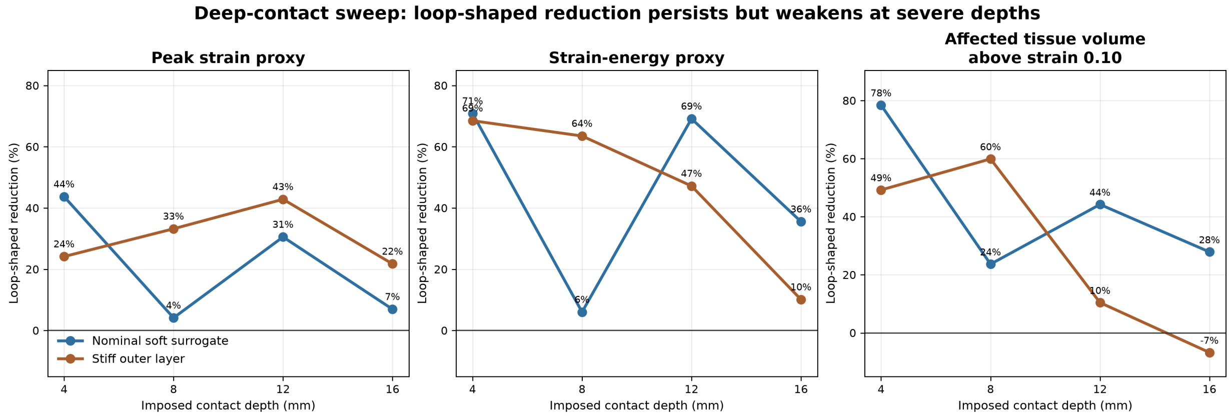

Figure 13: Deep-contact sweep across 4, 8, 12, and 16 mm imposed contact depths. Positive values indicate lower loop-shaped tissue-loading proxies relative to the matched conventional case. The reduction persists for the main continuous proxies, but weakens and becomes more threshold-sensitive at severe depths.

11.4 Laceration-Potential Severity Classes

FEBio contact cases were also summarized with transparent laceration-potential classes—not calibrated wound diagnoses, but a rule-based synthesis of p95 principal strain, p95 strain-energy density, high-strain tissue volumes, and imposed contact depth. Among conventional contact cases, 43% were classified severe/uncertain and 47% moderate, with only 3% low. Among loop-shaped cases, 10% were severe/uncertain, 30% moderate, and 47% low. One surprising result is how strongly the class distribution shifted: loop-shaped contact moved most cases into lower laceration-potential categories rather than merely trimming a continuous proxy. These classes summarize modeled tissue loading after contact and are not field-validated injury diagnoses.

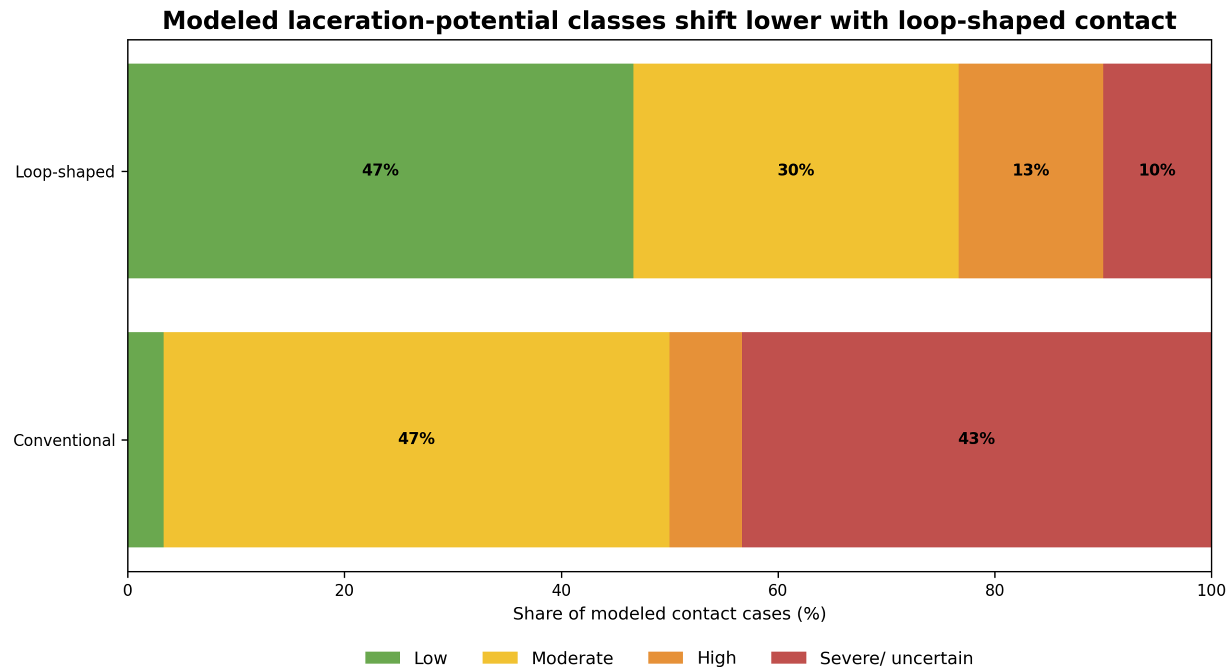

Figure 14: Rule-based laceration-potential class distribution across FEBio contact cases. Classes summarize modeled tissue loading and are intended for paired interpretation; they are not calibrated biological wound diagnoses.

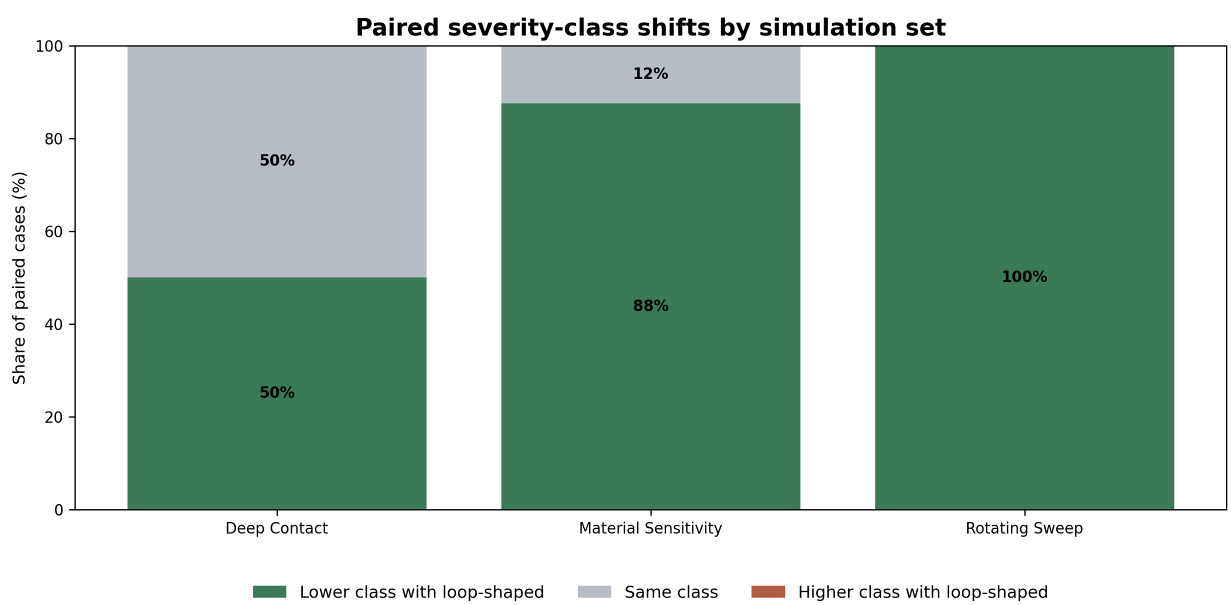

Figure 15: Paired severity-class shifts across rotating-sweep, material-sensitivity, and deep-contact simulation sets.

12 Expansion Analyses

Two postprocessing extensions reorganize existing outputs around candidate tissue-damage thresholds and cross-domain agreement among CAD, CFD, and FEBio results—calibration steps, not new biological validation.

12.1 Candidate Tissue-Damage Thresholds

FEBio contact outputs were reprocessed into candidate damage-threshold summaries: p95 strain, p95 stress, p95 strain-energy density, high-strain tissue volume, and a transparent candidate damage index

$$I_d = 0.35\,E_{95} + 0.35\,W_{95} + 0.30\frac{\log(1 + V_{\epsilon\geq 0.10})}{10},$$

where E_{95} is p95 absolute principal strain, W_{95} is p95 strain-energy density, and $V_{\epsilon\geq 0.10}$ is tissue volume above principal strain 0.10. This index is a placeholder for tissue-surrogate recalibration, not a biological injury law. At 4 mm contact the candidate damage index was 48.2% lower for loop-shaped geometry; at 8 mm, 58.9% lower.

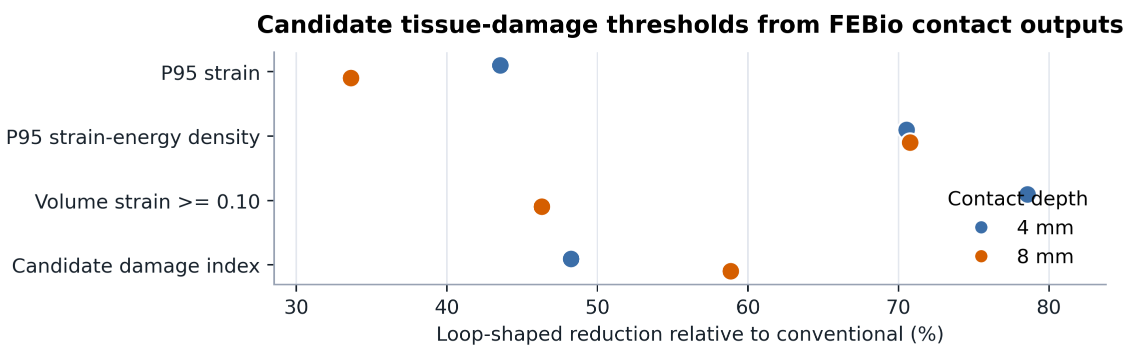

Figure 16: Candidate tissue-damage threshold reductions derived from FEBio contact outputs. These are calibration targets for future tissue-surrogate experiments, not final biological failure thresholds.

12.2 Joined Geometry–CFD–Contact Validation Dataset

CAD laceration profiles, sliding-mesh CFD summaries, and FEBio tissue-contact reductions were joined into one cross-domain table. CAD laceration profiles showed a median 33% lower loop-shaped laceration/contact proxy; FEBio tissue contact showed a median 55% lower tissue-loading proxy. CFD showed a median −32% loop-shaped difference across flow-field metrics—several quantities were lower for loop-shaped geometry, but CFD remains secondary because flow fields do not directly determine whether tissue is cut.

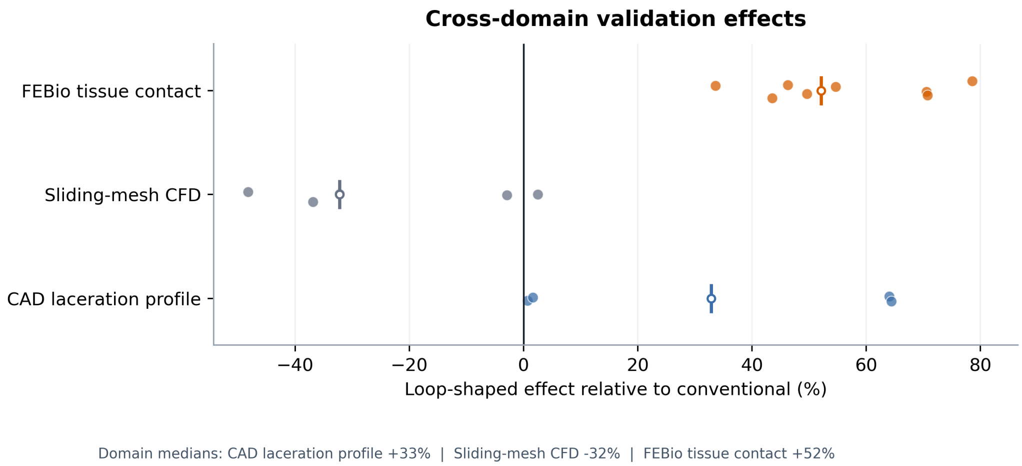

Figure 17: Cross-domain validation effects. Points are individual joined metrics; hollow markers mark domain medians. Positive values indicate lower loop-shaped laceration or tissue-contact proxies; negative CFD values indicate lower loop-shaped flow-field values.

13 Discussion

This prototype supports a conditional mechanistic hypothesis: loop-shaped propellers may reduce modeled laceration-relevant tissue loading relative to conventional propellers, primarily through blunter, less exposed edge geometry rather than large changes in encounter probability.

Three lines of evidence converge: matched Monte Carlo laceration runs show large edge-contact-factor differences with small contact-rate differences; FEBio rotating-sweep contact shows lower p95 strain, stress, strain-energy density, and high-strain tissue volume at matched depths; and the rule-based laceration-potential synthesis shifts more loop-shaped cases into lower loading classes. CFD is compatible but not decisive—sliding-mesh results show lower pressure- and turbulence-related field values while mean velocity is modestly higher.

The main limitation is input realism: conclusions ultimately depend on CAD-derived edge geometry propagating through contact, laceration scoring, and finite-element interpretation. Weighting sweeps confirm that default splits are not what force answers near 60–70%; geometry does. Future work should focus on validating section-fitted edge radii through physical metrology, expanding biomechanical calibration, and comparing modeled tissue-loading proxies with controlled tissue-surrogate experiments.

Selected References

Marine Animal Tissue, Trauma, and Contact Mechanics

- Geraci, J. R., and Lounsbury, V. J. (2005). *Marine Mammals Ashore: A Field Guide for Strandings*. 2nd ed. National Aquarium in Baltimore.
- Moore, M. J., et al. (2013). Criteria and case definitions for serious injury and death of pinnipeds and cetaceans caused by anthropogenic trauma. *Diseases of Aquatic Organisms*, 103(3), 229–264.

- Campbell-Malone, R., et al. (2008). Biomechanics of the right whale mandible: digital image correlation and finite element analysis. *Journal of Experimental Biology*, 211(24), 3999–4009.
- Fung, Y. C. (1993). *Biomechanics: Mechanical Properties of Living Tissues.* 2nd ed. Springer.
- Holzapfel, G. A. (2000). *Nonlinear Solid Mechanics: A Continuum Approach for Engineering.* Wiley.
- Vogel, S. (2003). *Comparative Biomechanics: Life's Physical World.* Princeton University Press.

Animal Behavior and Exposure

- Hartman, D. S. (1979). *Ecology and behavior of the manatee (Trichechus manatus) in Florida.*
- Edwards, H. H. et al. (2016). Influence of manatees' diving on their risk of collision with watercraft. *PLOS ONE.*
- Jaine, F. R. A. et al. (2012). When giants turn up: sighting trends, environmental influences and habitat use of the manta ray *Manta alfredi* at a coral reef. *PLOS ONE.*
- Braun, C. D. et al. (2014). Diving behavior of the reef manta ray links coral reefs with adjacent deep pelagic habitats. *PLOS ONE.*

Propeller Hydrodynamics and CFD Context

- Carlton, J. (2019). *Marine Propellers and Propulsion.* 4th ed. Butterworth-Heinemann.
- Breslin, J. P. and Andersen, P. (1994). *Hydrodynamics of Ship Propellers.* Cambridge University Press.
- Ferziger, J. H., Peric, M., and Street, R. L. (2020). *Computational Methods for Fluid Dynamics.* Springer.
- Versteeg, H. K. and Malalasekera, W. (2007). *An Introduction to Computational Fluid Dynamics: The Finite Volume Method.* Pearson.
- Menter, F. R. (1994). Two-equation eddy-viscosity turbulence models for engineering applications. *AIAA Journal*, 32(8), 1598–1605.
- Weller, H. G., Tabor, G., Jasak, H., and Fureby, C. (1998). A tensorial approach to computational continuum mechanics using object-oriented techniques. *Computers in Physics*, 12(6), 620–631.
- Zhang, B., Ding, C., and Liang, C. (2021). High-order implicit large-eddy simulation of flow over a marine propeller. *Computers & Fluids*, 224, 104967. `https://doi.org/10.1016/j.compfluid.2021.104967`.
- Zhang, Q., Jaiman, R. K., Ma, P., and Liu, J. (2019). Investigation on the performance of a ducted propeller in oblique flow. *Journal of Offshore Mechanics and Arctic Engineering*, 141(4), 041802. `https://doi.org/10.1115/1.4043943`.

Scientific Python and Software Tools

- Harris, C. R. et al. (2020). Array programming with NumPy. *Nature*, 585, 357–362.
- Virtanen, P. et al. (2020). SciPy 1.0: fundamental algorithms for scientific computing in Python. *Nature Methods*, 17, 261–272.
- McKinney, W. (2010). Data structures for statistical computing in Python. In *Proceedings of the 9th Python in Science Conference*, 56–61.
- Hunter, J. D. (2007). Matplotlib: A 2D graphics environment. *Computing in Science & Engineering*, 9(3), 90–95.
- Dawson-Haggerty et al. *trimesh*: Python tools for loading and using triangular meshes. `https://trimesh.org/`.
- The OpenFOAM Foundation. *OpenFOAM User Guide*. `https://openfoam.org/`.